Electronic Supplementary Material (ESI) for Journal of Materials Chemistry C.

Bead-Like Structures and Self-Assembled Monolayers from 2,6-Dipyrazolylpyridines and their Iron(II) Complexes

Laurynas Pukenas[a], Florence Benn[a], Edmund Lovell[a], Amedeo Santoro[b],
Laurence J. Kershaw Cook[b], Malcolm A. Halcrow*[b] and Stephen D. Evans*[a]

[a] *School of Physics and Astronomy, E. C. Stoner Building, University of Leeds, Leeds, UK LS2 9JT.*
[b] *School of Chemistry, University of Leeds, Woodhouse Lane, Leeds, UK LS2 9JT.*

E-mail: m.a.halcrow@leeds.ac.uk
s.d.evans@leeds.ac.uk;

Supporting Information

Synthetic procedures for the compounds in this work.

Scheme S1 Our previous synthesis of 4-(mercapto)-2,6-di(pyrazol-1-yl)pyridine (L^2), and the new procedure used in this study.

Scheme S2 Synthesis of 4-(*N*-thiomorpholinyl)-2,6-di(pyrazol-1-yl)pyridine (L^3).

Experimental details for the crystal structure data collections and refinements.

Table S1 Experimental details for the crystal structure determinations of the salts $[Fe(L^3)_2]X_2$.

Table S2 Selected bond lengths and angles in the crystal structures of the salts $[Fe(L^3)_2]X_2$.

Figure S1 View of the complex dication in the single crystal X-ray structure of $[Fe(L^3)_2][BF_4]_2 \cdot H_2O$, showing the full atom numbering scheme.

Scheme S3 Definition of the Jahn-Teller distortion parameters θ and ϕ.

Figure S2 Variable temperature magnetic susceptibility data for $[Fe(L^3)_2]X_2$ ($X^- = BF_4^-$, ClO_4^- and $CF_3SO_3^-$)

Figure S3 STM images of two chains of beads demonstrating kinks and changes of direction.

Figure S4 STM images of the ends of two different chains of beads.

Figure S5 STM images of a chain of beads associated with moiré patterns.

Figure S6 CITS current maps and *I*/*V* curves of a chain of beads associated with moiré patterns

Figure S7 The same *I*/*V* curves of the bead structures shown in Fig. 3 of the main article, showing the standard deviations of each *I*/*V* response.

Figure S8 Variable temperature XPS scans showing the binding energy of the Fe 2*p* peaks of films of $[Fe(bpp)_2][BF_4]_2$.

Figure S9 High resolution XPS spectra of L^2 on gold.

Table S3 Integrated peak areas and relative ratios of the elements in layers of L^2 on gold surfaces, derived from XPS data.

Table S4 Relative ratios of the chemical species in layers of L^2 on gold surfaces, derived from XPS data.

Table S5 Ellipsometry and contact angle data for SAMs of L^2.

Figure S10 High resolution XPS spectra of C *1s* region in SAM of L^3.

Figure S11 Possible binding mode of L^3 on a gold surface, from a molecular model based on the crystallographic structure of L^3 in its iron complexes.

Figure S12 XPS spectra of SAMs of L^3, before and after immersion in solutions of $Fe[ClO_4]_2$.

Figure S13 XPS spectra of SAMs of L^3 and its pre-formed iron complex.

References

Synthesis of compounds

Our previously published synthesis of *L*[2] involves reaction of 4-iodo-2,6-dipyrazolylpyridine with NaSH.[1] Although *L*[2] obtained by this route was pure by the standard chemical characterisation techniques, SAMs formed using this material contained iodine contaminents that were assumed to derive from trace iodine-containing impurities in the sample. Therefore, an alternative synthesis of *L*[2] was developed that does not involve iodine-containing reagents.

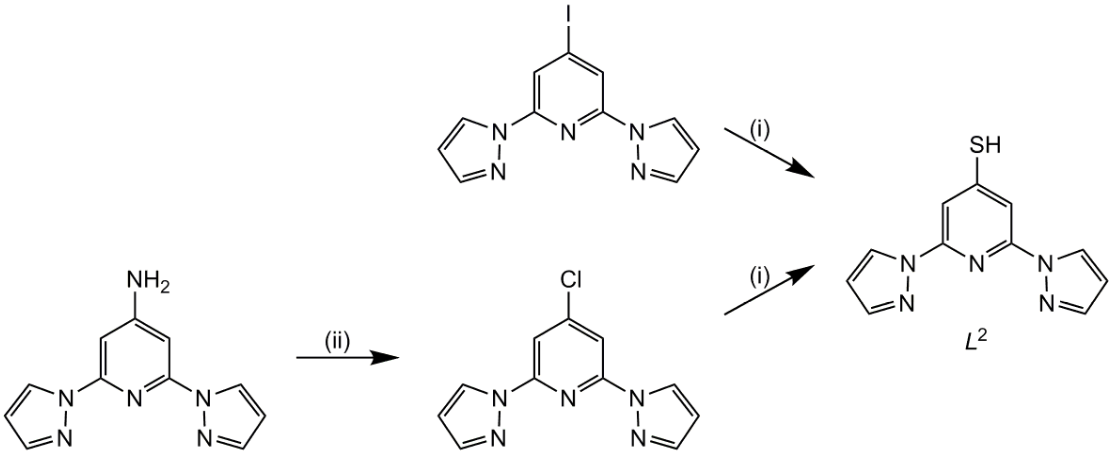

Scheme S1 Our previous synthesis of 4-(mercapto)-2,6-di(pyrazol-1-yl)pyridine (L^2),[1] and the new procedure used in this study. Reagents and conditions: (i) NaSH, dmf, reflux, 4 hrs then conc HCl. (ii) $NaNO_2$, KCl, HCl, MeCN 80 °C, 1 hr then $Na_2S_2O_3$ (aq).

Synthesis of 4-chloro-2,6-di(pyrazol-1-yl)pyridine. A stirred acetonitrile (30 cm^3) suspension of 4-amino-2,6-di(pyrazol-1-yl)pyridine[2] (0.41 g, 1.8 mmol) and sodium nitrite (0.26 g, 3.75 mmol) was stirred under N_2. Solid KCl (0.34 g, 4.5 mmol) was added, followed by the dropwise addition of 37% HCl (10 cm^3, 101.5 mmol) which caused the appearance of a bright orange colour. The contents were heated to 80 °C for 1 h, then cooled to room temperature. The light yellow solution was poured into saturated aqueous sodium thiosulfate (100 cm^3), and the mixture was shaken to afford a pale yellow solid. This was collected by filtration, washed with water and dried *in vacuo*. The white solid compound was purified by silica gel column chromatography (dichloromethane eluent, R_f 0.55). Yield 0.21 g, 48 %. Found C, 53.7; H, 3.40; N, 28.5 %. Calcd for $C_{11}H_8ClN_5$ C, 53.8; H, 3.28; N, 28.5 %. ES mass spectrum *m*/*z* 268.0 ($[Na(L)]^+$). ^1H NMR ($CDCl_3$) δ 6.52 (dd, 2.6 and 1.7 Hz, 2H, Pz H^4), 7.78 (d, 1.7 Hz, 2H, Pz H^3), 7.90 (s, 2H, Py $H^{3/5}$), 8.54 (d, 2.6 Hz, 2H, Pz H^5).

Synthesis of 4-(mercapto)-2,6-di(pyrazol-1-yl)pyridine (L^2). A mixture of 4-chloro-2,6-di(pyrazol-1-yl)pyridine (0.10 g, 0.41 mmol) and $NaSH \cdot H_2O$ (0.64 g, 8.6 mmol) in dimethylformamide (25 cm^3) was refluxed for 4 hrs, then cooled to room temperature. The turquoise solution was poured into water (200 cm^3), and filtered. The filtrate was neutralised with concentrated HCl, which precipitated an off-white solid which was collected by filtration, washed with water and dried *in vacuo*. Yield 63 mg, 64 %. Analytical and spectroscopic characterisation data from this material were consistent with our previous report.[1]

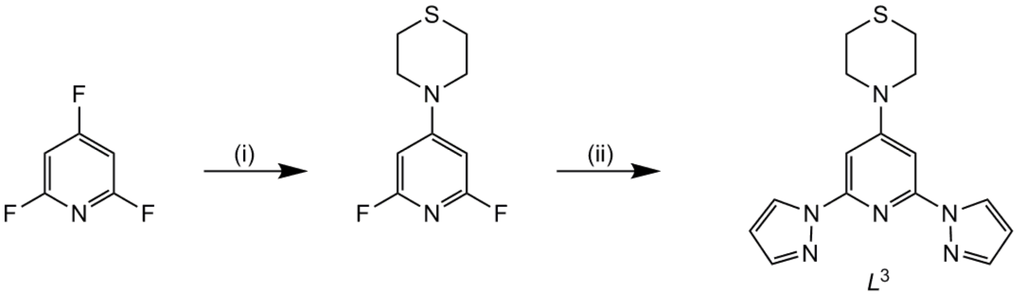

Scheme S2 Synthesis of the new ligand 4-(*N*-thiomorpholinyl)-2,6-di(pyrazol-1-yl)pyridine (L^3). Reagents and conditions: (i) thiomorpholine (1.1 equiv), NEt_3, ethanol, rt, 1 hr. (ii) Na[pyrazolide] (3 equiv), dmf, 100 °C, 12 hr.

Synthesis of 4-(N-thiomorpholinyl)-2,6-difluoropyridine. 2,4,6-Trifluoropyridine (1.0 g, 7.5 mmol) was dissolved in ethanol (25 cm^3). A solution of thiomorpholine (0.85 g, 8.3 mmol) and triethylamine (1.2 cm^3) in ethanol (5 cm^3) was then added, and the mixture was stirred for 1 hr at room temperature. Excess water was then added, resulting in a white precipitate which was collected, and washed thoroughly with water and hexane. The product was analysed without further purification. Yield 0.61 g, 37 %. Found C, 49.8; H, 4.60; N 12.9 %. Calcd for $C_9H_{10}F_2N_2S$ C, 50.0; H, 4.66; N, 13.0 %. ^1H NMR ($CDCl_3$) δ 2.68 (m, 4H, NCH_2CH_2S), 3.79 (m, 4H, NCH_2CH_2S), 6.05 (s, 2H, Py $H^{3/5}$). ^{13}C NMR ($CDCl_3$) δ 14.2 (NCH_2CH_2S), 65.2 (NCH_2CH_2S), 92.7 (m, Py $C^{3/5}$), 161.5 (dd, 232 and 20 Hz, 2C Py $C^{2/6}$), 171.8 (t, 13 Hz, Py C^4). ES mass spectrum *m*/*z* 217.1 ($[M+H]^+$), 239.1 ($[M+Na]^+$).

Synthesis of 4-(*N*-thiomorpholinyl)-2,6-di(pyrazol-1-yl)pyridine (L^3). Pyrazole (0.46 g, 6.8 mmol) was slowly added to a suspension of NaH (60 wt % in mineral oil; g, 6.8 mmol) in dry, anaerobic dmf (cm^3). After the effervescence had ceased, 4-(*N*-thiomorpholinyl)-2,6-difluoropyridine (0.49 g, 2.27 mmol) was added to the mixture, which was then heated under N_2 at 100 °C for 12 hrs. After cooling, the product was precipitated from the reaction mixture by addition of excess water, yielding an off-white solid that was filtered and washed with water and diethyl ether. Recrystallisation of the dried material from acetone/hexanes yielded a white solid. Yield 0.55 g, 77 %. %. Found C, 57.5; H, 5.30; N 26.6 %. Calcd for $C_{15}H_{16}N_6S$ C, 57.7; H, 5.16; N, 26.9 %. ES mass spectrum *m*/*z* 313.1 ($[HL^3]^+$), 335.1 ($[Na(L^3)]^+$), 647.2 ($[Na(L^3)_2]^+$). ^1H NMR ($CDCl_3$) δ 2.67 (m, 4H, NCH_2CH_2S), 3.89 (m, 4H, NCH_2CH_2S), 6.40 (pseudo-t, 2.0 Hz, 2H, Pz H^4), 7.17 (s, 2H, Py $H^{3/5}$), 7.68 (d, 1.8 Hz, 2H, Pz H^3), 8.52 (d, 2.4 Hz, 2H, Pz H^5).

Synthesis of the complexes $[Fe(L^3)_2]X_2$ (X = BF_4^-, ClO_4^- and $CF_3SO_3^-$). A mixture of L^3 (0.10 g, 0.32 mmol) and the appropriate iron(II) salt (0.16 mmol) was stirred in nitromethane (20 cm^3) until all the solid had dissolved. The resultant yellow solutions were concentrated to *ca.* 5 cm^3 volume, then filtered. Slow diffusion of diethyl ether vapour into these solutions yielded well-formed single crystals of the complex salts. Elemental analyses:

For $[Fe(L^3)_2][BF_4]_2\cdot H_2O$. Found C, 41.2; H, 3.80; N, 19.1 %. Calcd for $C_{30}H_{32}B_2F_8FeN_{12}S_2\cdot H_2O$ C, 41.3; H, 3.93; N, 19.3 %.

For $[Fe(L^3)_2][ClO_4]_2\cdot H_2O$. Found C, 40.4; H, 3.70; N, 18.7 %. Calcd for $C_{30}H_{32}Cl_2FeN_{12}O_8S_2\cdot H_2O$ C, 40.2; H, 3.82; N, 18.7 %.

For $[Fe(L^3)_2][CF_3SO_3]_2$. Found C, 39.2; H, 3.30; N, 16.9 %. Calcd for $C_{32}H_{32}F_6FeN_{12}O_6S_4$ C, 39.3; H, 3.30; N, 17.2 %.

Single crystal structure determinations

Diffraction data were measured with an Agilent Supernova dual-source diffractometer, using monochromated Mo-K_α radiation (λ = 0.7107 Å). Experimental details of the structure determination are given in Table S1. The structures were all solved by direct methods *(SHELXS97*[3]), and developed by full least-squares refinement on F^2 (*SHELXL97*[3]). Crystallographic figures were prepared using *XSEED*,[4] which incorporates *POVRAY*.[5] Unless otherwise stated, all crystallographically ordered non-H atoms in these structures were refined anisotropically, while C-bound H atoms were placed in calculated positions and refined using a riding model.

The same anion in the BF_4^- and ClO_4^- salt structures is disordered over two sites, with a refined occupancy ratio of 0.67:0.33. In **[Fe(L^3)$_2$][BF$_4$]$_2$**·H_2O, modelling this anion disorder required the use of refined B–F and F…F distance restraints. The water molecule, which hydrogen bonds to the disordered anion, was fully occupied in the model. The water H atoms were located in the Fourier map and refined with the fixed restraints O–H = 0.90(2) and H...H = 1.47(2) Å, and with $U_{\mathrm{iso}}\{\mathrm{H}\}$ = 1.5x $U_{\mathrm{iso}}\{\mathrm{O}\}$. CCDC 1058749.

The disordered anion in **[Fe(L^3)$_2$][ClO$_4$]$_2$**·$x$$H_2O$ was modelled successfully without restraints. In contrast to the BF_4^- salt, the lattice water site [O(56)] in this structure is only partially occupied according to its displacement parameter. The anion disorder apparently correlates with the presence or absence of this water site, so O(56) was refined with the same occupancy as the minor disorder residue in the final least squares cycles. All non-H atoms except the minor anion disorder site were refined anisotropically. Although the partial H atoms associated with the water site could not be located or refined, the water H content is included in the density and *F*000 calculations. CCDC 1058750.

No disorder is present in **[Fe(L^3)$_2$][CF$_3$SO$_3$]$_2$**, and no restraints were applied to the model. CCDC 1058751.

Table S1 Experimental details for the crystal structure determinations of the salts [Fe(L^3)$_2$]X$_2$ (X^- = BF_4^-, ClO_4^- and $CF_3SO_3^-$) .

	[Fe(L^3)$_2$][BF$_4$]$_2$·H_2O	**[Fe(L^3)$_2$][ClO$_4$]$_2$**·$x$$H_2O$ ($x \approx 0.33$)	**[Fe(L^3)$_2$][CF$_3$SO$_3$]$_2$**
Molecular formula	$C_{30}H_{34}B_2F_8FeN_{12}OS_2$	$C_{30}H_{32.66}Cl_2FeN_{12}O_{8.33}S_2$	$C_{32}H_{32}F_6FeN_{12}O_6S_4$
M_r	872.28	885.49	978.79
Crystal class	triclinic	triclinic	triclinic
Space group	$P\bar{1}$	$P\bar{1}$	$P\bar{1}$
a (Å)	11.4182(5)	11.5334(6)	12.4186(7)
b (Å)	13.3351(7)	13.2237(7)	13.3433(7)
c (Å)	13.8880(8)	14.0842(8)	14.2652(6)
α (°)	85.289(4)	85.594(4)	75.472(4)
β (°)	68.183(4)	68.230(5)	67.419(5)
γ (°)	66.115(4)	65.418(5)	64.190(5)
V (Å^3)	1789.21(16)	1806.40(17)	1954.89(17)
Z	2	2	2
T (K)	100(2)	100(2)	100(2)
μ (mm^{-1})	0.627	0.751	0.690
Measured reflections	13966	21938	11920
Independent reflections	8281	8768	8652
R_{int}	0.037	0.065	0.033
R_1, $I > 2\sigma(I)$[a]	0.056	0.058	0.052
wR_2, all data[b]	0.142	0.116	0.119
Goodness of fit	1.054	1.046	1.038

[a] $R = \Sigma[|F_o| - |F_c|] / \Sigma|F_o|$. [b] $wR = [\Sigma w(F_o^2 - F_c^2) \ / \ \Sigma w F_o^4]^{1/2}$

Table S2 Selected bond lengths and angles in the crystal structures of the salts $[Fe(L^3)_2]X_2$ ($X^- = BF_4^-$, ClO_4^- and $CF_3SO_3^-$). See Fig. S1 for the atom numbering scheme, and Scheme S3 for the definitions of θ and ϕ.

	$\mathbf{[Fe(L^3)_2][BF_4]_2}\cdot H_2O$	$\mathbf{[Fe(L^3)_2][ClO_4]_2}\cdot xH_2O$ ($x \approx 0.33$)	$\mathbf{[Fe(L^3)_2][CF_3SO_3]_2}$
Fe(1)–N(2)	2.115(2)	2.119(2)	2.128(2)
Fe(1)–N(9)	2.206(2)	2.207(2)	2.200(3)
Fe(1)–N(14)	2.167(2)	2.167(2)	2.180(3)
Fe(1)–N(24)	2.109(2)	2.107(2)	2.135(2)
Fe(1)–N(31)	2.189(2)	2.180(2)	2.182(2)
Fe(1)–N(36)	2.228(2)	2.227(2)	2.209(2)
N(2)–Fe(1)–N(9)	73.25(9)	72.93(9)	72.80(9)
N(2)–Fe(1)–N(14)	72.33(9)	72.63(9)	72.34(9)
N(2)–Fe(1)–N(24) (ϕ)	162.78(9)	163.22(9)	161.95(9)
N(2)–Fe(1)–N(31)	92.22(9)	93.65(9)	92.27(9)
N(2)–Fe(1)–N(36)	121.61(9)	120.05(9)	123.36(9)
N(9)–Fe(1)–N(14)	142.82(9)	143.31(9)	142.59(9)
N(9)–Fe(1)–N(24)	115.30(9)	117.23(9)	117.11(9)
N(9)–Fe(1)–N(31)	93.25(9)	94.21(9)	95.80(9)
N(9)–Fe(1)–N(36)	99.90(9)	99.47(9)	95.23(9)
N(14)–Fe(1)–N(24)	101.65(9)	99.27(9)	100.14(9)
N(14)–Fe(1)–N(31)	101.65(9)	100.22(9)	98.70(9)
N(14)–Fe(1)–N(36)	86.52(9)	87.05(9)	92.71(9)
N(24)–Fe(1)–N(31)	72.91(9)	72.98(9)	72.32(9)
N(24)–Fe(1)–N(36)	73.06(9)	73.10(9)	72.49(9)
N(31)–Fe(1)–N(36)	145.93(9)	146.02(9)	144.38(9)
θ	86.41(3)	88.04(3)	85.95(3)

The Fe–N bond lengths in each structure are within the ranges expected for a high-spin complex of this type.[6] There are only minor differences in the molecular structures of the complex between the structures, which is unsurprising since the three salts are essentially isostructural (Table S1).

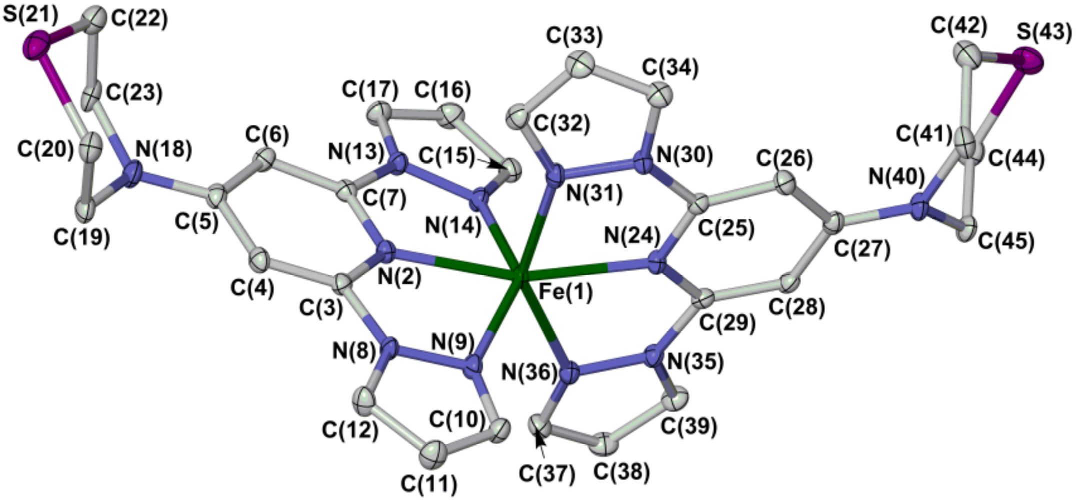

Figure S1 View of the complex dication in the single crystal X-ray structure of $[Fe(L^3)_2][BF_4]_2 \cdot H_2O$, showing the full atom numbering scheme. Displacement ellipsoids are at the 50 % probability level, and H atoms have been omitted for clarity. The view is the same as in Fig. 5 of the main article.

Colour code: C, white; Fe, green; N, blue; S, purple.

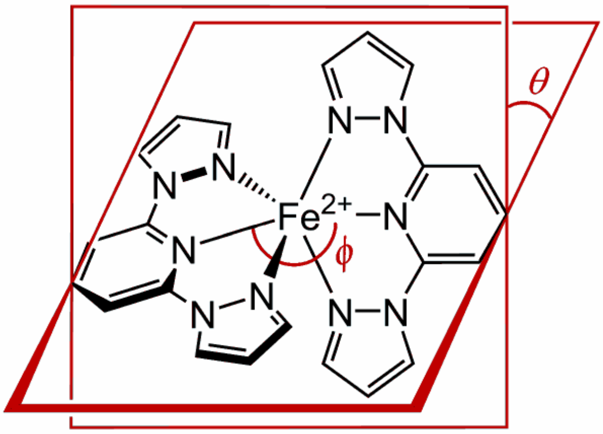

Scheme S3 Definition of the distortion parameters θ and ϕ (Table S2).

These parameters define the magnitude of an angular Jahn-Teller distortion, that is often observed in high-spin $[Fe(bpp)_2]^{2+}$ derivatives ($\theta \leq 90º$, $\phi \leq 180$ º).[7] Spin-crossover is inhibited if θ and ϕ deviate too far from their ideal values, because the associated rearrangement to a more regular low-spin coordination geometry ($\theta \approx 90º$, $\phi \approx 180º$) cannot be accommodated by a rigid solid lattice.[6,8]

Solid complexes with $\phi < 172°$ and/or $\theta < 76°$ usually remain trapped in their high-spin form on cooling[6] (although there are a small number of exceptions[9]). The low values of ϕ for $[Fe(L^3)_2]^{2+}$ in the crystal structures in this work [$161.95(9) \leq \phi \leq 163.22(9)°$] imply it should be spin-crossover inactive, as observed (Fig. S2).

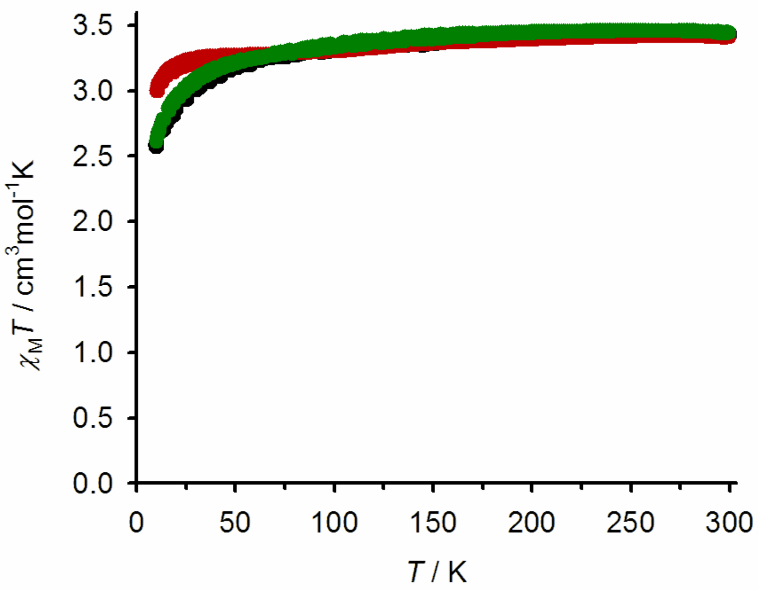

Figure S2 Variable temperature magnetic susceptibility data for powder samples of $[Fe(L^3)_2]X_2$ ($X^- = BF_4^-$ [black], ClO_4^- [green] and $CF_3SO_3^-$ [red]).

All three compounds are high-spin in the solid state between 10-300 K. The slight decrease in $\chi_M T$ at low temperatures reflects zero field splitting of the high-spin $^5T_{2g}$ spin manifold (in O_h symmetry), and is not related to spin-crossover.

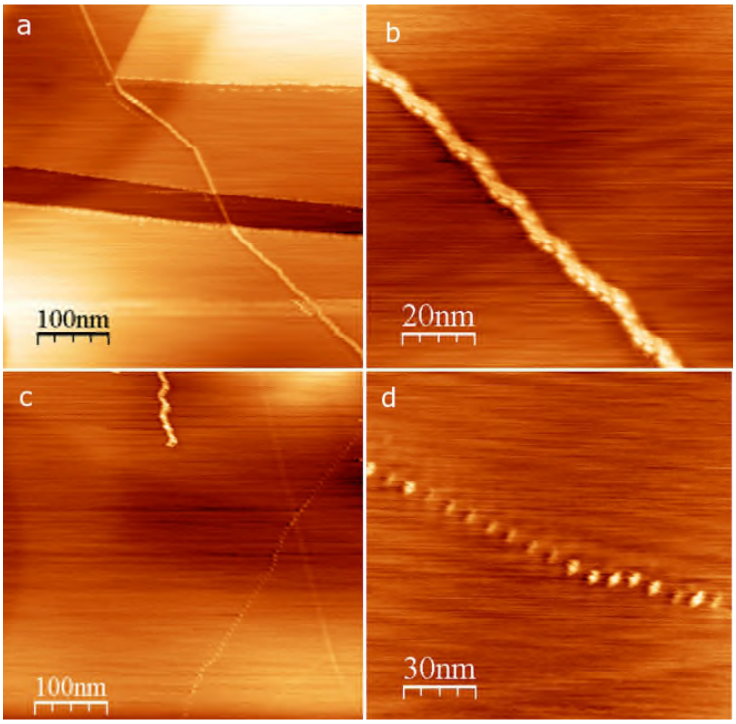

Figure S3. (a), (b) STM images of the same chain of touching beads at different magnifications. (c), (d) STM images of a different chain of well-separated beads at two magnifications. Both these chains of beads demonstrate kinks and changes of direction at different, but consistent, angles (156 ±1° for the top chain, 113 ±2° for the bottom chain).

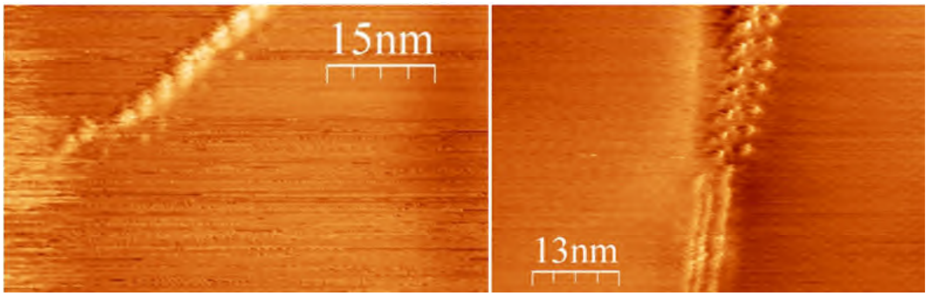

Figure S4. STM images of the ends of two different chains of beads. Left: the chain peters out on an apparently flat region of HOPG substrate. Right: a chain runs off a series of step edges on the surface.

Although the image on the right suffers from a double STM tip, the different structure of the chain end is clearly evident.

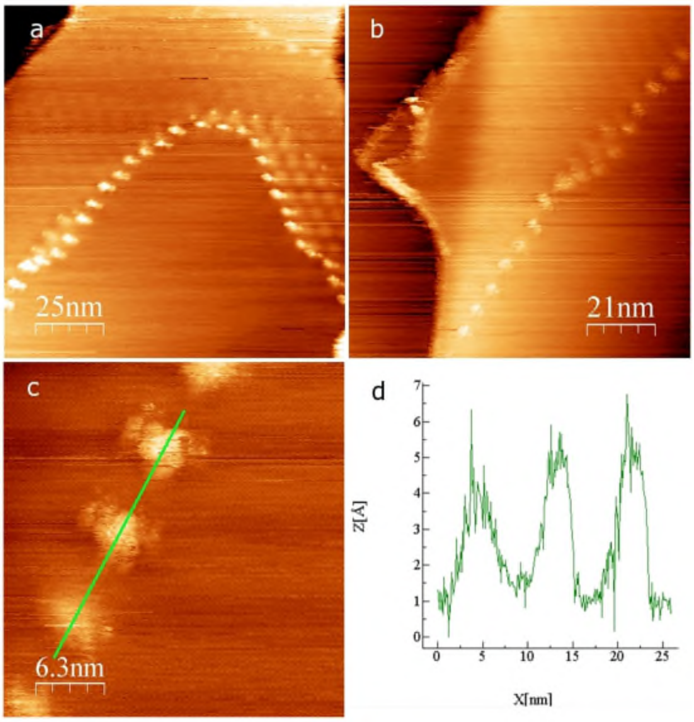

Figure S5. (a)-(c) STM images of a chain of beads associated with moiré patterns on the HOPG surface, at different magnifications, and (d) the profile over the three central beads in (c) showing widths of 5 nm and heights of 4-5 Å.

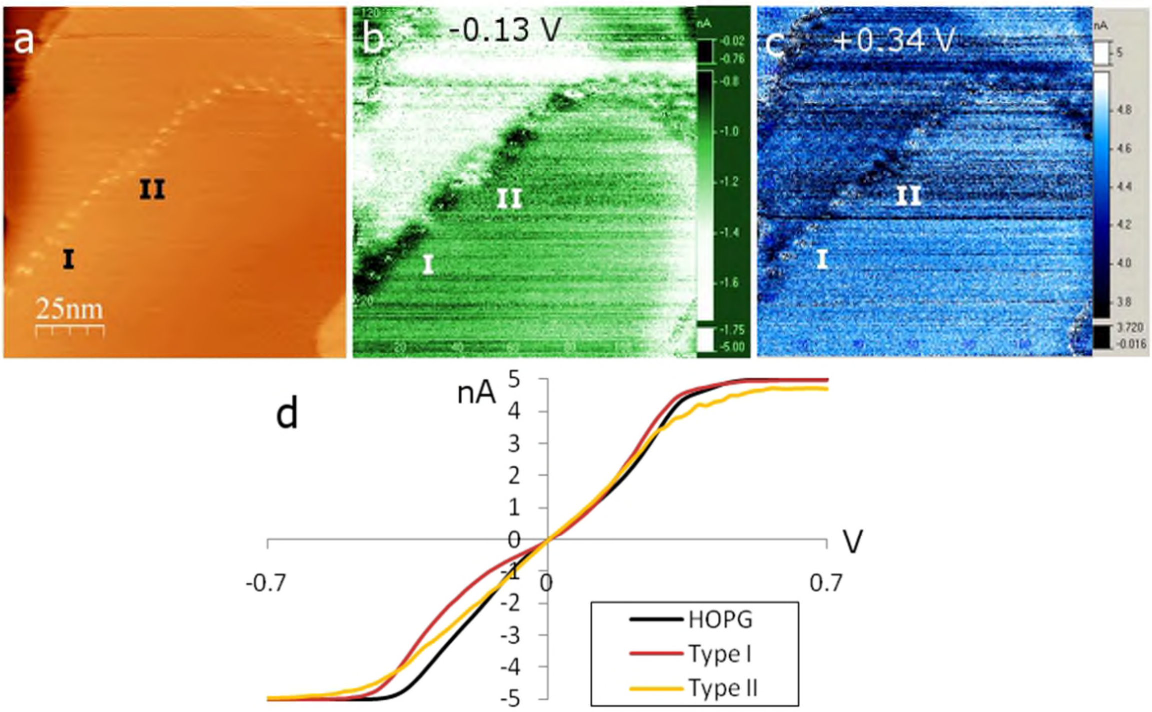

Figure S6. A topographic scan of the features in Fig. S5, with CITS current maps at (b) –0.13 V and (c) +0.34 V. (d) The average corresponding current-voltage curves over an area of the HOPG in the bottom half of the image, at the centre of one of the type I and one of the type II beads.

The bead structures are clearly distinct from the moiré patterns in both types of image.

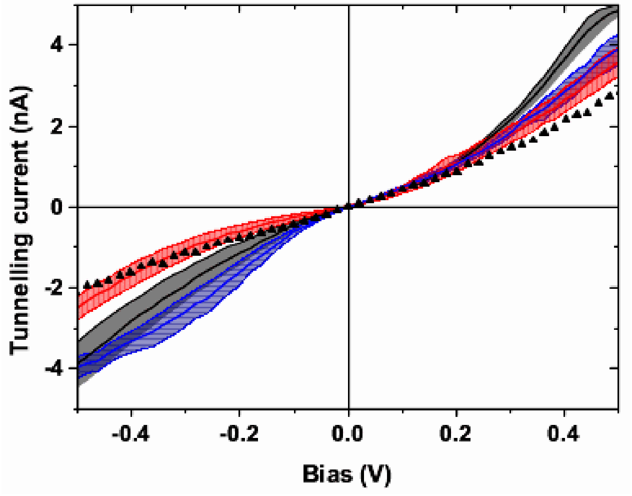

Figure S7 The same *I*/*V* curves of the bead structures shown in Fig. 3 of the main article, showing the standard deviations of each *I*/*V* response. Black line, substrate; red line, type I beads (average of ten beads); blue line, type II beads (average of 6 beads); black triangles, a type III bead observed to possibly switch at negative bias in the STM images (data from just one bead).

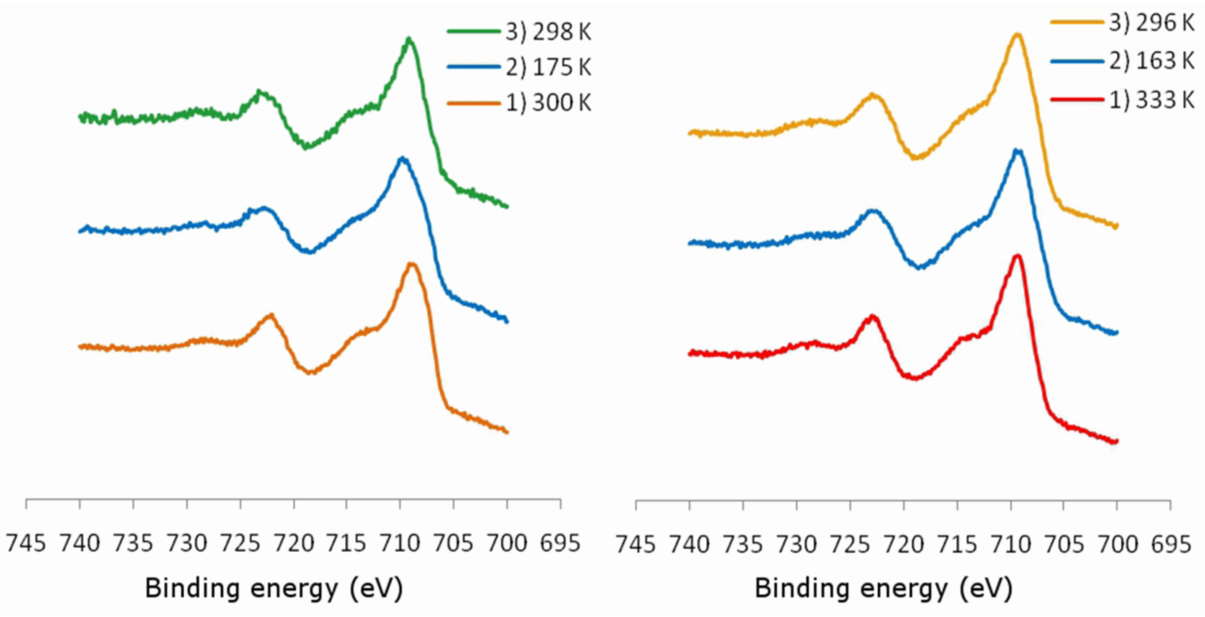

Figure S8 XPS scans showing the binding energy of the Fe 2*p* peaks of films of $[Fe(bpp)_2][BF_4]_2$, at temperatures either side of its spin-transition. A spin-transition should lead to a reduction in the more intense $2p_{3/2}$ binding energy in the low temperature spectra by *ca* 1 eV, and also to a reduction in intensity of the satellite peaks.[10] That is not observed in these data.

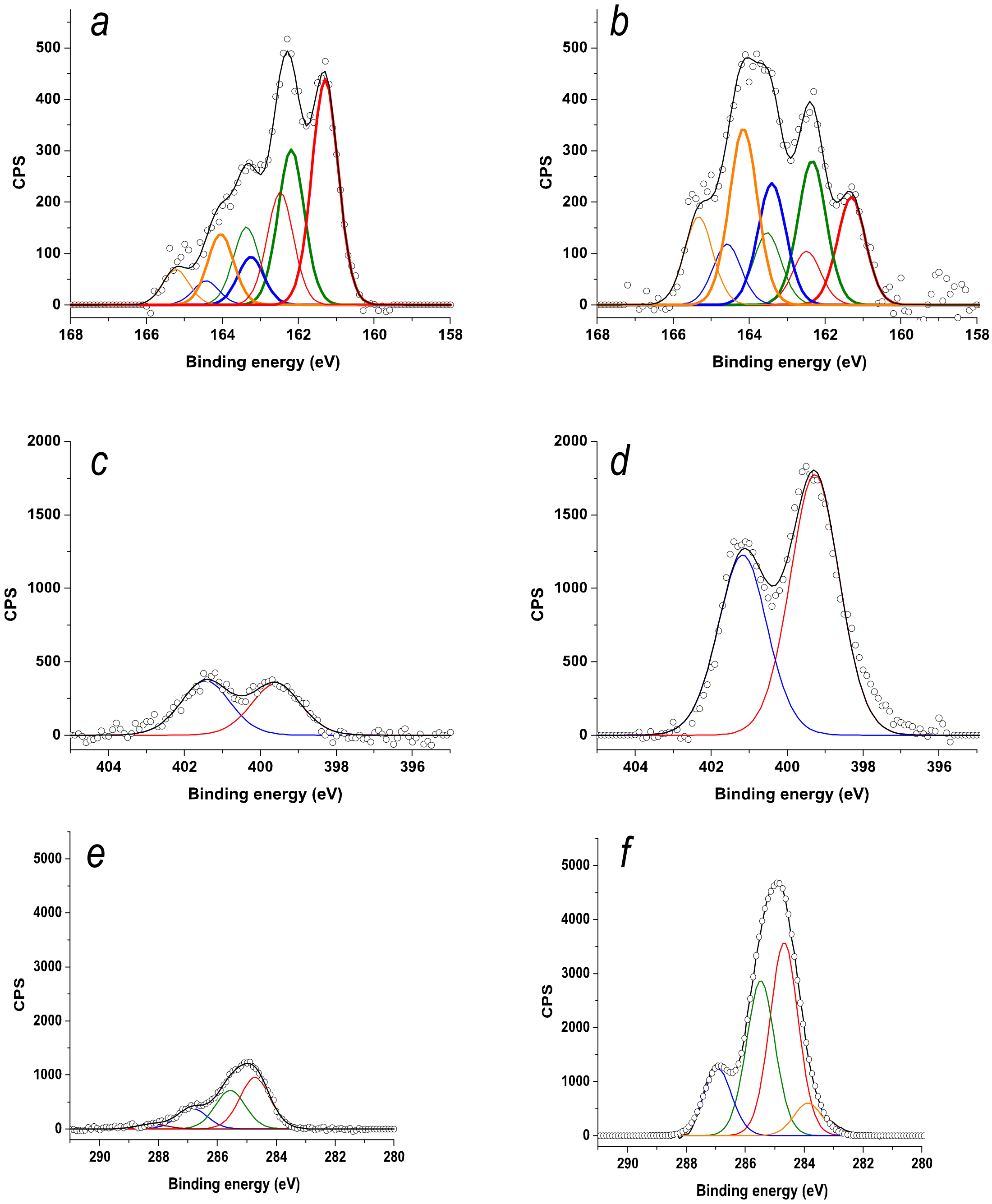

Figure S9 High resolution XPS spectra of L^2 on gold. Binding energies and relative ratios of the components in (a)-(f) are shown in Table S4.

(a) S *2p* spectrum of SAM; (b) S *2p* spectrum of drop-cast film. Both regions show presence of four distinct chemical species of sulfur: elemental (red), thiolates (green), unbound thiols (blue), partially oxidised sulphur (orange), where the thick lines correspond to $2p_{3/2}$ peaks.

c) N 1*s* spectrum of SAM; (d) N 1*s* spectrum of drop-cast film. The red component corresponds to binding energy of nitrogen in pyridine and nitrogen in 2^{nd} position in pyrazole rings, while the blue line is assigned to nitrogen in 1st position in pyrazoles.

(e) C 1*s* spectrum of SAM; (f) C 1*s* spectrum of drop-cast film.

(a)-(e) correspond to SAMs or drop-cast films from ethanol solution, while (f) is from a sample drop-cast from dichloromethane.

[a]While experimental data of C 1s regions are similar for all the films produced by drop-casting, small changes in C 1s shape strongly affected the outcome of the fitted peaks. Carbon region of the film drop-cast from DCM was selected as a better representative curve showing relative ratios of the components (2 : 5 : 6) somehow comparable to the expected values (2 : 3 : 6), according to the proposed model in literature (see Table S4).

All SAMs of L^2 show the presence of four sulfur species as shown in Figure S9a, although the relative ratios of those species vary between samples (Table S3). Also, there is significantly less elemental sulfur in drop-cast films on gold compared to the SAMs. While drop-cast films yield a ratio very close to 2:3 of blue and red components in N 1s region, respectively, SAMs show these peaks with similar intensities. Although S *2p* regions suggest comparable amount of sulfur in both samples, there is significantly less nitrogen and carbon in the SAM.

Table S3 Integrated (and normalised using relative sensitivity factors) peak areas and relative ratios of the elements in layers of L^2 on gold surfaces, derived from XPS data.

Solvent	Au 4*f*	S 2*p*	C 1*s*	C:S ratio	N 1*s*	N:S ratio	O 1*s*	O:S ratio
Drop-cast								
CH_2Cl_2	9.9	1.5	16.3	11.2	4.7	3.2	0.7	0.5
EtOH	9.8	1.7	12.7	7.6	3.9	2.3	0.6	0.4
MeCN	6.7	1.9	17.1	8.8	5.3	2.7	1.0	0.5
SAMs								
CH_2Cl_2	17.8	1.4	4.9	3.5	0.9	0.7	0.5	0.4
EtOH	12.0	1.3	4.6	3.5	1.0	0.8	0.6	0.5
MeCN	14.6	1.3	5.4	4.2	1.0	0.8	0.9	0.7
Expected values				11		5		0

Table S4 Relative ratios of the chemical species in layers of L^2 on gold surfaces, derived from XPS data.

Solvent	Fraction of total S *2p* region				Pyrrolic : pyridinic N ratio
	Elemental S	Thiolates	Unbound thiols	Partially oxidised S	
Binding energy[a] (eV)	161.3 ± 0.1	162.2 ± 0.1	163.3 ± 0.1	164.1 ± 0.1	401.3 ± 0.2 : 399.4 ± 0.2
Drop-cast					
CH_2Cl_2	0.2	0.2	0.1	0.5	2.0 : 2.7
EtOH	0.2	0.3	0.2	0.3	2.0 : 2.9
MeCN	0.1	0.2	0.3	0.4	2.0 : 3.3
SAMs					
CH_2Cl_2	0.5	0.4	0.1	0.1	2.0 : 1.9
EtOH	0.5	0.3	0.1	0.1	2.0 : 1.9
MeCN	0.5	0.3	0.1	0.1	2.0 : 1.7
Expected values	0.0	1.0 [b]	0.0 [b]	0.0	2.0 : 3.0

[a] Binding energies are referenced to Au 4*f* 7/2 at 83.9 eV. Stated values were averaged over the samples listed in the table and quoted errors correspond to standard deviations.

Carbon components at 284.2 ± 0.2 eV, 285.3 ± 0.2 eV and 286.8 ± 0.1 eV were present in all our films containing bpp or its derivatives. According a literature model,[11] they could be respectively assigned to **C 1s - A** (pyridyl *C*3/5, pyrazolyl *C*3 and *C*5), **C 1s - B** (pyridyl *C*4 and pyrazolyl *C*4) and **C 1s - C** (pyridyl *C*2/6). Two low intensity components at 283.3 ± 0.5 eV and 288.5 ± 0.2 eV were present in some samples, but are not unexpected.

Although binding energies, number of components and their relative ratios varied across the samples, that does not necessarily indicate varying species of carbon or their relative amounts in the samples. It's more likely to result from the sensitivity of fitting procedure to small changes in the shape of C 1s region containing species with closely overlapping binding energies. **Consequently, the relative ratios of these carbon components should be interpreted with caution.**

[b]Applicable to SAMs only.

Table S5 Ellipsometry and contact angle data for SAMs of L^2. All SAMs were produced from 1 mM solutions of L^2, unless otherwise indicated.

Solvent	Thickness (Å)	Advancing angle (°)	Receding angle (°)
CH_2Cl_2	13 ± 2	89 ± 1	49 ± 3
dmf	3 ± 0.3	90 ± 4	35 ± 5
EtOH	13 ± 1 (16 ± 1[a])	77 ± 2 (79 ± 3 [a])	41 (33 ± 2 [a])
MeCN	34 ± 3	79 ± 2	33 ± 2

[a]Solution concentration 10 mM.

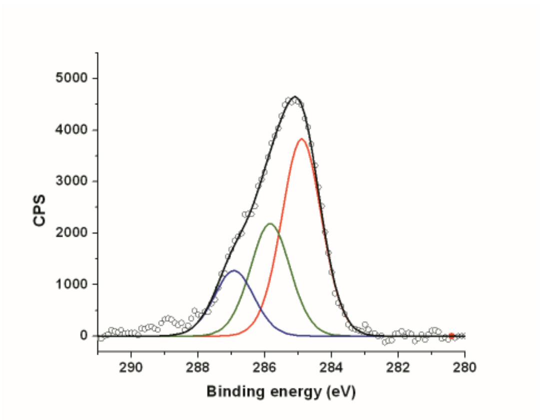

Figure S10 High resolution XPS spectra of C *1s* region in SAM of L^3. Fitted components at 284.9 eV, 285.8 eV and 286.9 eV have similar binding energies to [Fe(bpp)$_2$][BF$_4$]$_2$ and [Fe(L^1)$_2$][BF$_4$]$_2$ films.

Peak positions are shifted slightly towards higher binding energy, if compared to **C 1s – A**, **C 1s – B** and **C 1s – C**, and show relative ratios close to 2 : 3 : 6.

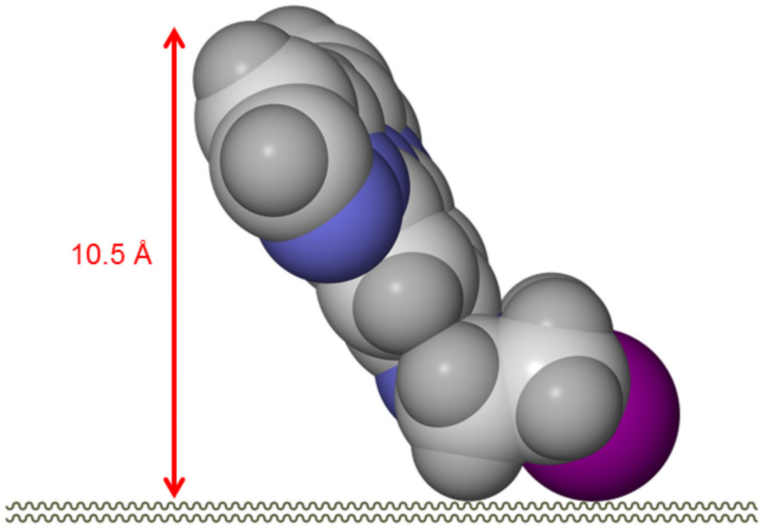

Figure S11 Possible binding mode of L^3 on a gold surface, from a molecular model based on the crystallographic structure of L^3 in its iron complexes.

The distance shown is in reasonable agreement with the thickness of the SAM from ellipsometry data (7.9-8.9 ± 1 Å). An alternative binding mode, with the bpp fragment oriented towards the gold surface, leads to a much smaller layer thickness of *ca* 5.5 Å.

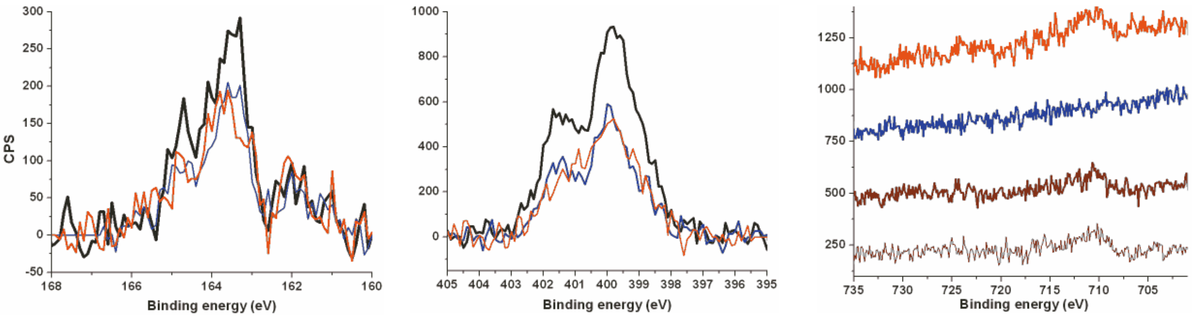

Figure S12 XPS spectra of SAMS of L^3 , before and after immersion in solutions of $Fe[ClO_4]_2$, in the S *2p* (left), N *1s* (middle) and Fe *2p* (right) regions. The black, blue and red lines correspond to SAM of L^3 that was untreated, immersed for 1 min. and immersed for 30 min. into 5mM $Fe[ClO_4]_2$ acetonitrile solution, respectively.

The thin and thick brown lines in Fe 2p spectra correspond to clean gold substrate immersed for 1min. and for 30 min., respectively, into the same $Fe[ClO_4]_2$ solution. The amounts of iron detected on SAM of L^3 are comparable to those on clean gold substrate and fall far below the level that would be expected for a single Fe ion per molecule in SAM of L^3.

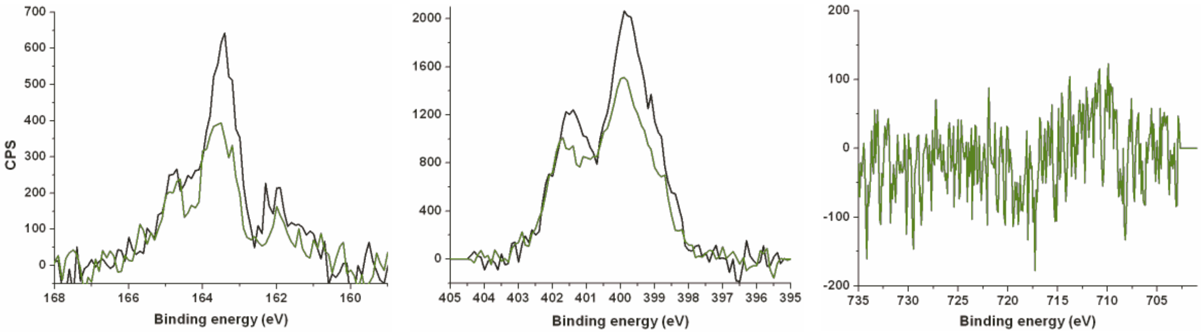

Figure S13 XPS spectra of SAMs L^3 and its pre-formed iron complex in the S *2p* (left), N *1s* (middle) and Fe *2p* (right) regions. The black and green lines correspond to SAM of L^3 and SAM formed in solution of the pre-formed SCO complex $[Fe(L^3)_2][ClO_4]_2$, respectively.

No indication of a significant amount of iron, and similar S *2p* and N *1s* spectra, suggest that a SAM of metal-free L^3 is formed from $[Fe(L^3)_2][ClO_4]_2$ solutions.

References.

1 L. J. Kershaw Cook, J. Fisher, L. P. Harding and M. A. Halcrow, *Dalton Trans.*, 2015, **44**, 9417.

2 C. Rajadurai, F. Schramm, S. Brink, O. Fuhr, M. Ghafari, R. Kruk and M. Ruben, *Inorg. Chem.*, 2006, **45**, 10019.

3 G. M. Sheldrick, *Acta Crystallogr., Sect. A*, 2008, **64**, 112

4 L. J. Barbour, *J. Supramol. Chem.*, 2001, **1**, 189.

5 *POVRAY*, v. 3.5, Persistence of Vision Raytracer Pty. Ltd., Williamstown, Victoria, Australia, 2002. http://www.povray.org.

6 M. A. Halcrow, *Coord. Chem. Rev.*, 2009, **253**, 2493.

7 J. M. Holland, J. A. McAllister, C. A. Kilner, M. Thornton-Pett, A. J. Bridgeman and M. A. Halcrow, *J. Chem. Soc., Dalton Trans.*, 2002, 548.

8 L. J. Kershaw Cook, R. Mohammed, G. Sherborne, T. D. Roberts, S. Alvarez and M. A. Halcrow, *Coord. Chem. Rev.*, 2015, **289–290**, 2.

9 L. J. Kershaw Cook, F. L. Thorp-Greenwood, T. P. Comyn, O. Cespedes, G. Chastanet and M. A. Halcrow, *Inorg. Chem.*, under revision and refs therein.

10 L. N. Mazalov, I. P. Asanov and V. A. Varnek, *J. Electron Spectrosc. Rel. Phenom.*, 1998, **96**, 209.

11 C. Shen, M. Haryono, A. Grohmann, M. Buck, T. Weidner, N. Ballav and M. Zharnikov, *Langmuir*, 2008, **24**, 12883.